2010

Discrete Coordinate Transformation for Designing All-Dielectric Flat Antennas

Wenxuan Tang
University of London

Christos Argyropoulos
University of London, christos.argyropoulos@unl.edu

Efthymios Kallos
University of London

Wei Song
Beijing Institute of Technology

Yang Hao
University of London

Discrete Coordinate Transformation for Designing All-Dielectric Flat Antennas

Wenxuan Tang, *Student Member, IEEE*, Christos Argyropoulos, *Student Member, IEEE*, Efthymios Kallos, Wei Song, and Yang Hao, *Senior Member, IEEE*

***Abstract*—Transformation electromagnetics provides a practical approach to control electromagnetic fields at will. Based on this principle, novel devices such as the invisible cloak have been proposed. Here we examine the extension of this technique as applied to the design of flat devices in antenna systems. A method using discrete coordinate transformation is proposed, which allows the conversion of conventional devices with curved shapes into flat systems, while preserving their non-dispersive, isotropic, broadband, and lossless properties. Two specific design examples, a flat reflector and a flat lens embedded in free space, are presented. To avoid the loss and narrow bandwidth issues typically present in metamaterials, appropriate approximations and simplifications are introduced to make the all-dielectric devices, which are more practical to build. It is also shown that the discrete coordinate transformation is valid for both the E and H polarizations, as long as the local coordinates of the system remain near-orthogonal. Finite-Difference Time-Domain simulations are used to verify the performances of these designs, and show that the all-dielectric devices have similar broadband performances compared to the conventional ones, while possessing the advantages of flat profiles and small volumes.**

***Index Terms*—Antennas, all-dielectric metamaterials, dispersion, FDTD, flat lens, flat reflector, transformation electromagnetics.**

I. Introduction

TRANSFORMATION electromagnetics has developed dramatically since it was proposed a few years ago [1], [2]. This technique provides a methodology to control the propagation of the electromagnetic waves by carefully adjusting the material parameters of space. Let's assume a 3D volume of space described by a cartesian coordinate system (x, y, z), and a second volume described by a distorted coordinate system (x', y', z'). 2D cut-planes in those spaces are shown in Fig. 1. The two coordinate systems are related through a general transformation function $x' = x'(x, y, z)$, $y' = y'(x, y, z)$, $z' = z'(x, y, z)$. An incident electromagnetic wave (illustrated for clarity purposes as a ray with arrow) travels along a path in both coordinate systems. In the cartesian coordinate system, we assume its path to be a straight line. In the distorted coordinate system, the ray path is distorted according to the mesh defined by the distorted coordinates. Maxwell's equations are form-invariant under coordinate transformations, but have different material parameters in different coordinate systems. As a result, if in the initial system space is isotropic and homogeneous, in the distorted system the permittivity and permeability will no longer hold these properties. Their distribution is predicted mathematically by the distortion of space derived from the coordinate transformation function between the two systems [3]. In practical applications the inverse procedure is actually desirable: one can theoretically design the (distorted) propagation characteristics of a traveling electromagnetic wave, and subsequently engineer a medium with the necessary material parameters to achieve the specific behavior. For example, in Fig. 1(a) the incoming wave will impinge on the object drawn in gray, but will avoid it [Fig. 1(b)] by perceiving a distorted space generated by the appropriate tuning of the material parameters.

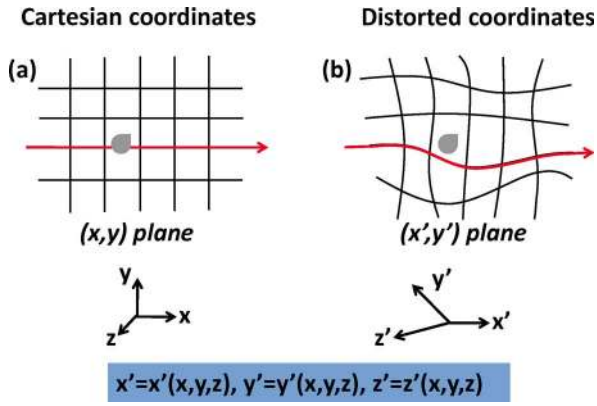

Fig. 1. Two coordinate systems. (a) The Cartesian coordinates and (b) the distorted coordinates. The incident electronic waves travel from point to point in both the two coordinates, but their routes are different. In the distorted coordinate, the wave will not reach the gray object.

This technique was first utilized in the design of the invisibility cloak [1]. In this scenario the incident waves, which initially propagate parallel to a straight line, are guided smoothly around an object before their original path is restored, thus hiding the object's existence from an outside observer. The original inhomogeneous anisotropic space with the object is the physical space and the homogeneous isotropic space without the object (which is perceived by the waves ideally as free space) is the virtual space. Different types of cloaks have been proposed [3]–[6] and experimental verification of an approximate device has been demonstrated at microwave frequencies [7]. Other coordinate transformation applications

Manuscript received February 25, 2010; revised May 25, 2010; accepted May 31, 2010. Date of publication September 23, 2010; date of current version November 30, 2010.

W. Tang, C. Argyropoulos, E. Kallos, and Y. Hao are with the Department of Electronic Engineering, Queen Mary, University of London, London E1 4NS, U.K. (e-mail: yang.hao@elec.qmul.ac.uk).

W. Song was with Department of Electronic Engineering, Queen Mary, University of London, London E1 4NS, U.K.. She is now with the Center for Electromagnetic Simulation, School of Information Science and Technology, Beijing Institute of Technology, Beijing 100081, China.

Color versions of one or more of the figures in this paper are available online at http://ieeexplore.ieee.org.

Digital Object Identifier 10.1109/TAP.2010.2078475

have also been examined in the literature, such as the electromagnetic concentrators, the field rotators, the wave conversion devices, the high-directivity antennas, etc. [8]–[14]. However, practically implementing most of these devices has turned out to be challenging, because the required material parameters from the transformations produce regions of space where complicated values of permittivity and permeability are required. Although artificially fabricated structures of metamaterials have proven capable of providing unusual range of permittivity and permeability values not found in nature [15], [16], they complicate the design process and are usually accompanied by high losses and narrow bandwidths, originating from the inevitably dispersive nature of metamaterials. Besides, the required materials resulting from transformation electromagnetics are usually anisotropic, which makes material practical realization very difficult.

In order to circumvent some of the limitations of metamaterials, more recently the idea of a simplified yet limited in performance cloak has been suggested, i.e., the ground-plane cloak [17]. In the initial scenario, an object is concealed in a small region above a ground plane, as shown in the top half of Fig. 2. A discrete coordinate transformation is applied to map the physical space with the object on the plane to a virtual space without any object above the plane. Without using a continuous transformation function, each distorted cell in the physical space is mapped numerically to an orthogonal cell in the virtual space. For certain structures, by choosing a proper grid in the curved space, one can generate near-orthogonal meshes which lead to isotropic material properties with minimal impact on the cloaking performance. As a result, they have equal tensor elements which can be made using conventional materials. This minimization of anisotropy is possible because the original design of the ground-plane cloak requires significantly less bending and distortion of the incident waves, due to the presence of the ground plane. As we shall also demonstrate in this paper, generating nearly isotropic material parameters is possible in general whenever the design of a metamaterial device does not impose extreme behavior onto the electromagnetic waves. Due to the simplified material parameters, various versions of the ground-plane cloak have been demonstrated experimentally both in microwave as well as infrared frequencies [18]–[21].

In this paper we extend the above principles into the design of simpler antenna systems by examining the inverse process. Instead of transforming a distorted coordinate system in the physical space into an orthogonal coordinate system in the virtual space, we transform a distorted coordinate system in the virtual space into an orthogonal coordinate system in physical space (as shown in the bottom half of Fig. 2). For example, in antenna systems, many widely used devices have curved shapes, such as parabolic reflectors and convex lenses. Using the coordinate transformation, we can design equivalent devices that operate in the same manner but have much more convenient flat shapes instead of curved ones. This is achieved as follows. In the virtual space perceived by the electromagnetic waves the devices have curved edges, have homogeneous and isotropic material parameters, and are described by distorted coordinate systems. These distorted coordinate systems are mapped using

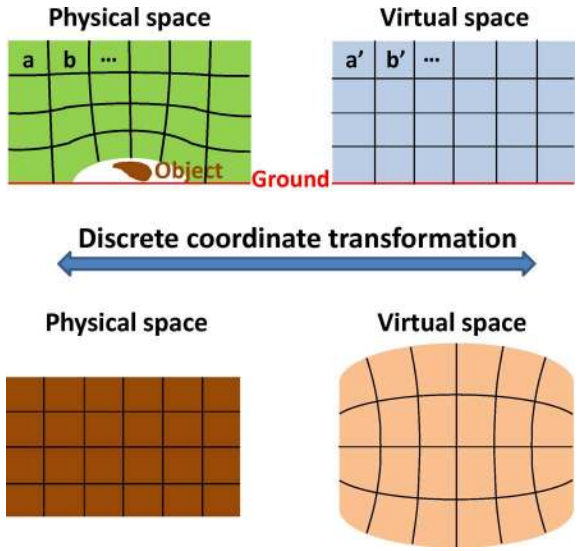

Fig. 2. The discrete coordinate transformation. The transformation is operated between each pair of the local coordinate system (a and a', b and b', etc.) in the physical space and the virtual space.

appropriate transformations to the physical space where the devices have flat edges, have inhomogeneous and isotropic material parameters, and are described by orthogonal coordinate systems. The material parameters in the physical systems are derived from the discrete coordinate transformation, and after minimizing their anisotropy [17] and simplifying their design [22], are shown through Finite-Difference Time-Domain (FDTD) simulations to perform as well as the conventional curved devices. In addition, the resulting devices are all-dielectric, lossless and broadband, and therefore can be easily constructed without the need of complex metamaterial structures in the same manner as the ground-plane cloak described earlier.

Certain types of flat lenses have been previously proposed [23], [24]. In these cases, the general coordinate transformation functions are used to calculate the electromagnetic parameters, and the lenses have dispersive permittivity map and permeability map simultaneously. More recently, quasi-conformal transformation optics has been proposed to produce a flat Luneburg lens [25]. In that work, the flat lens is made by patterning copper strips on an FR4 substrate to realize the required refractive index map. The technique presented here generates lenses that only have dispersive permittivity map. With appropriate simplification, the lenses are built up easily by a few blocks of dielectrics.

In the rest of the paper, we first describe the underlying mathematical principles of the discrete coordinate transformation proposed. Then, the method is used to design a flat reflector and a flat focusing lens. Their design is then simplified to consist of only a few blocks of all-dielectric materials, which is much easier to build practically. 2D FDTD simulations of those designs confirm that their performances are as good as the performances of their conventional curved-shaped counterparts. We anticipate that the proposed technique could be extended in the future to more practical applications and other devices as well.

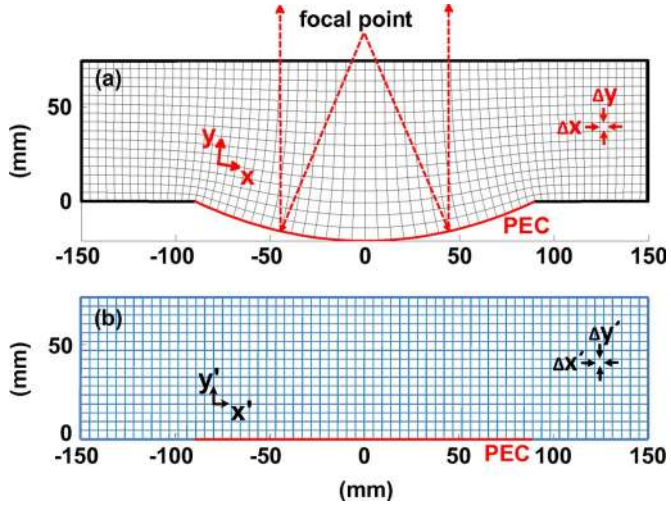

Fig. 3. (a) The virtual space with distorted coordinates. A reflector is set in the air, as illustrated by the bottom curve. (b) The physical space with Cartesian coordinates. The curved reflector is replaced with a flat PEC sheet at the bottom.

II. The Discrete Coordinate Transformation

In this section we present the main theoretical principles behind the discrete coordinate transformation. The method can be applied to many conventional devices that do not have sharp boundaries. For illustrative purposes we show here the example of metallic parabolic reflector embedded in free space. The virtual space of the device is shown in Fig. 3(a). The physical space is shown in Fig. 3(b) which is a flat metallic sheet surrounded by a distribution of dielectric material. In both spaces, an incident from the top electromagnetic wave will be focused at the focal point of the device.

Suppose that the coordinate transformation between the virtual space and the physical space is $x' = x'(x,y,z)$, $y' = y'(x,y,z)$, $z' = z'(x,y,z)$, where (x,y,z) are the local coordinates in the virtual space and (x',y',z') are the local coordinates in the physical space. According to the theory of transformation electromagnetics [3], the resulting permittivity and permeability tensors in the physical space are given by

$$\bar{\bar{\varepsilon}}' = \frac{J\bar{\bar{\varepsilon}}J^T}{\det(J)}, \bar{\bar{\mu}}' = \frac{J\bar{\bar{\mu}}J^T}{\det(J)}. \tag{1}$$

Here $\bar{\bar{\varepsilon}}$ and $\bar{\bar{\mu}}$ are the permittivity and permeability tensors in the original virtual space, and J is the Jacobian transformation matrix between the two coordinate systems, defined as

$$J = \begin{pmatrix} \frac{\partial x'}{\partial x} & \frac{\partial x'}{\partial y} & \frac{\partial x'}{\partial z} \\ \frac{\partial y'}{\partial x} & \frac{\partial y'}{\partial y} & \frac{\partial y'}{\partial z} \\ \frac{\partial z'}{\partial x} & \frac{\partial z'}{\partial y} & \frac{\partial z'}{\partial z} \end{pmatrix}. \tag{2}$$

Assuming that the reflector is surrounded by free space in the virtual space, the original permittivity and permeability tensors are

$$\bar{\bar{\epsilon}} = \varepsilon_0 \mathbf{I} \tag{3}$$

$$\bar{\bar{\mu}} = \mu_0 \mathbf{I} \tag{4}$$

where $\mathbf{I}$ is the unitary matrix.

For simplification purposes we now assume that the transformation is 2-dimensional, and thus the device is infinite in the z direction normal to the xy plane. In the 2D case, the Jacobian matrix has a simpler form

$$J = \begin{pmatrix} \frac{\partial x'}{\partial x} & \frac{\partial x'}{\partial y} & 0 \\ \frac{\partial y'}{\partial x} & \frac{\partial y'}{\partial y} & 0 \\ 0 & 0 & 1 \end{pmatrix} \tag{5}$$

and (1) is explicitly written as

$$\bar{\bar{\varepsilon}}' = \varepsilon_0 \frac{\begin{pmatrix} \left(\frac{\partial x'}{\partial x}\right)^2 + \left(\frac{\partial x'}{\partial y}\right)^2 & \frac{\partial x'}{\partial x}\frac{\partial y'}{\partial x} + \frac{\partial x'}{\partial y}\frac{\partial y'}{\partial y} & 0 \\ \frac{\partial y'}{\partial x}\frac{\partial x'}{\partial x} + \frac{\partial x'}{\partial y}\frac{\partial y'}{\partial y} & \left(\frac{\partial y'}{\partial x}\right)^2 + \left(\frac{\partial y'}{\partial y}\right)^2 & 0 \\ 0 & 0 & 1 \end{pmatrix}}{\det(J)} \tag{6}$$

$$\bar{\bar{\mu}}' = \mu_0 \frac{\begin{pmatrix} \left(\frac{\partial x'}{\partial x}\right)^2 + \left(\frac{\partial x'}{\partial y}\right)^2 & \frac{\partial x'}{\partial x}\frac{\partial y'}{\partial x} + \frac{\partial x'}{\partial y}\frac{\partial y'}{\partial y} & 0 \\ \frac{\partial y'}{\partial x}\frac{\partial x'}{\partial x} + \frac{\partial x'}{\partial y}\frac{\partial y'}{\partial y} & \left(\frac{\partial y'}{\partial x}\right)^2 + \left(\frac{\partial y'}{\partial y}\right)^2 & 0 \\ 0 & 0 & 1 \end{pmatrix}}{\det(J)}. \tag{7}$$

For an E-polarized incident wave (electric field along the z direction), only the components μ_{xx}, μ_{xy}, μ_{yy}, μ_{yx} and ε_{zz} contribute. In that case the permittivity and permeability become

$$\varepsilon'_z \equiv \varepsilon'_{zz} = \varepsilon_0 \det(J)^{-1} \tag{8}$$

$$\bar{\bar{\mu}}' = \mu_0 \frac{\begin{pmatrix} \left(\frac{\partial x'}{\partial x}\right)^2 + \left(\frac{\partial x'}{\partial y}\right)^2 & \frac{\partial x'}{\partial x}\frac{\partial y'}{\partial x} + \frac{\partial x'}{\partial y}\frac{\partial y'}{\partial y} \\ \frac{\partial y'}{\partial x}\frac{\partial x'}{\partial x} + \frac{\partial x'}{\partial y}\frac{\partial y'}{\partial y} & \left(\frac{\partial y'}{\partial x}\right)^2 + \left(\frac{\partial y'}{\partial y}\right)^2 \end{pmatrix}}{\det(J)}. \tag{9}$$

Based on the theoretical study in [17], for anisotropic materials an effective average refractive index n' can be defined as

$$\begin{aligned} n'^2 &= n'_{xx}n'_{yy}/(\varepsilon_0\mu_0) \\ &= \sqrt{\mu'_{yy}\varepsilon'_z}\sqrt{\mu'_{xx}\varepsilon'_z}/(\varepsilon_0\mu_0) = \sqrt{\mu'_{yy}\mu'_{xx}}\varepsilon'_z/(\varepsilon_0\mu_0) \end{aligned} \tag{10}$$

where μ'_{xx} and μ'_{yy} are the principal values of the permeability tensor in (9) and n'_{xx} and n'_{yy} are the corresponding principal values of the refractive index tensor.

Equation (10) indicates that if $\mu'_{xx}\mu'_{yy} = \mu_0^2$, i.e., if there is no magnetic dependence, then the refractive index n', which determines the trace of the wave, could be realized by the permittivity alone, leading to an all-dielectric device. Next, we shall show that this condition is approximately satisfied if a certain grid is properly selected in the coordinate transformation.

The explicit value of $\mu'_{xx}\mu'_{yy}$ from (9) is

$$\begin{aligned} \mu'_{xx}\mu'_{yy} = \mu_0^2 \Bigg[& \left(\frac{\partial x'}{\partial x}\right)^2 \left(\frac{\partial y'}{\partial x}\right)^2 \\ & + \left(\frac{\partial x'}{\partial x}\right)^2 \left(\frac{\partial y'}{\partial y}\right)^2 + \left(\frac{\partial x'}{\partial y}\right)^2 \left(\frac{\partial y'}{\partial x}\right)^2 \\ & + \left(\frac{\partial x'}{\partial y}\right)^2 \left(\frac{\partial y'}{\partial y}\right)^2 \Bigg] \Bigg/ \Bigg[\left(\frac{\partial x'}{\partial x}\right)^2 \left(\frac{\partial y'}{\partial y}\right)^2 \\ & - 2\frac{\partial x'}{\partial x}\frac{\partial y'}{\partial y}\frac{\partial x'}{\partial y}\frac{\partial y'}{\partial x} + \left(\frac{\partial x'}{\partial y}\right)^2 \left(\frac{\partial y'}{\partial x}\right)^2 \Bigg]. \end{aligned} \tag{11}$$

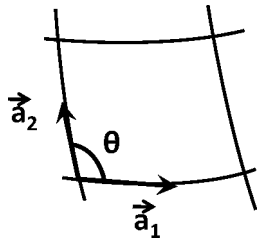

Fig. 4. The covariant base vectors in a 2D sample distorted cell.

The approximate condition $\mu'_{xx}\mu'_{yy} \simeq \mu_0^2$ is satisfied when at the same time

$$\frac{\partial x'}{\partial y} \simeq 0 \tag{12}$$

$$\frac{\partial y'}{\partial x} \simeq 0. \tag{13}$$

Since x' and y' are functions of both x and y, (12) and (13) can be also written using the chain rule as

$$\frac{\partial x'}{\partial y} = \frac{\partial x'}{\partial x}\frac{\partial x}{\partial y} \simeq 0 \tag{14}$$

$$\frac{\partial y'}{\partial x} = \frac{\partial y'}{\partial y}\frac{\partial y}{\partial x} \simeq 0. \tag{15}$$

However, the above condition can indeed be satisfied because we can generate a grid in the virtual space with near-orthogonal cells such that

$$\frac{\partial x}{\partial y} \simeq 0 \tag{16}$$

$$\frac{\partial y}{\partial x} \simeq 0. \tag{17}$$

To illustrate how this orthogonality restriction can be approximately satisfied, see for example the virtual space shown in Fig. 3(a). A sample distorted cell is drawn in Fig. 4, which is characterized by the 2×2 covariant metric g [26]–[28]

$$g = \begin{pmatrix} g_{11} & g_{12} \\ g_{21} & g_{22} \end{pmatrix} \tag{18}$$

$$g_{i,j} = \vec{a}_i \cdot \vec{a}_j (i,j = 1,2) \tag{19}$$

where $\vec{a}_1$ and $\vec{a}_1$ are the covariant base vectors defined in Fig. 4, and θ is the angle between them.

We quantify the orthogonality of the grid using the parameter θ for each cell, defined through

$$\cos\theta = \sqrt{\frac{g_{12}g_{21}}{g_{11}g_{22}}}. \tag{20}$$

The distribution of the angle parameter θ is plotted in Fig. 5 for the grid shown in Fig. 3(a). We observe that most cells are indeed near-orthogonal and are distributed around the 90° point, with a smaller number of cells further away from 90°. We also measure from this graph the full width at half maximum (FWHM) of the distribution. Thus, for a perfectly orthogonal grid, g is a unit matrix, $\cos\theta = 0$, FWHM $= 0$, and ultimately $\mu'_{xx}\mu'_{yy} = \mu_0^2$. However, even for a near-orthogonal grid such as the one in Fig. 3(a), these conditions can be approximately satisfied, yielding an all-dielectric device with very minor sacrifice in performance.

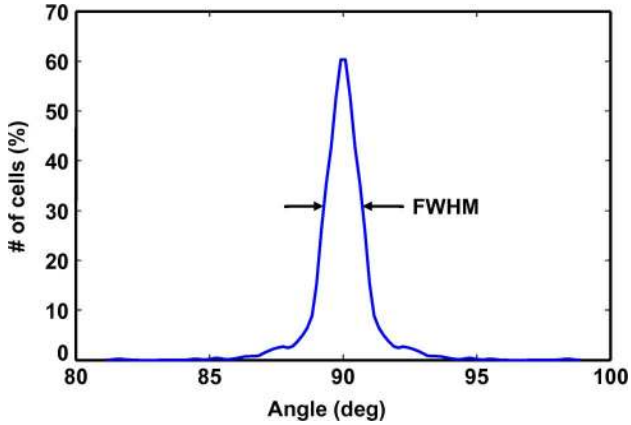

Fig. 5. The distribution of the degrees between two local coordinates in every grid of the virtual space. The orthogonal property is quantified by the full width at half maximum (FWHM) index. When the FWHM index is approaching zero, the local coordinates are near-orthogonal. In this case the index is only 1°, indicating that the local coordinates are near-orthogonal.

Furthermore, the near-orthogonal property ensures an approximation of (9) that

$$\bar{\bar{\mu}}' = \mu_0 \frac{\begin{pmatrix} \left(\frac{\partial x'}{\partial x}\right)^2 & 0 \\ 0 & \left(\frac{\partial y'}{\partial y}\right)^2 \end{pmatrix}}{\det(J)}. \tag{21}$$

Because all meshes are generated to be approximately square shaped, μ'_{xx} and μ'_{yy} have similar values and the permeability matrix has equal tensor elements which are equal to unity, as that in the free space.

Accordingly, the relative permeability of the device can be assumed to be isotropic and unity, and the effective relative refractive index in (10) is only dependent on ε'_z

$$n'^2 \simeq \varepsilon'_z/\varepsilon_0 = \frac{1}{\det(J)}. \tag{22}$$

Note that under the orthogonal condition of (12) and (13), the refractive index profile of the device can be directly retrieved from the cells of the generated grid, using (5)

$$n'^2 \simeq \frac{1}{\frac{\partial x'}{\partial x}\frac{\partial y'}{\partial y}} \simeq \frac{\Delta x \Delta y}{\Delta x' \Delta y'} \tag{23}$$

where $\Delta x, \Delta y, \Delta x', \Delta y'$ are the dimensions of each cell in the two coordinate systems as shown in Fig. 3.

For the case of H polarization, similar results are obtained. Now the contributing components of the permittivity and permeability are ε_{xx}, ε_{xy}, ε_{yy}, ε_{yx} and μ_{zz}, as seen in (6) and (7). Under the orthogonality criteria of (12) and (13), the permittivity and permeability tensors become

$$\bar{\bar{\varepsilon}}' = \varepsilon_0 \frac{\begin{pmatrix} \left(\frac{\partial x'}{\partial x}\right)^2 & 0 \\ 0 & \left(\frac{\partial y'}{\partial y}\right)^2 \end{pmatrix}}{\det(J)}, \quad \mu'_z = \mu_0 \det(J)^{-1} \tag{24}$$

while $\det(J) = (\partial x')/(\partial x) \cdot (\partial y')/(\partial y)$. The effective refractive index is now

$$n'^2 = n'_{xx} n'_{yy}/(\varepsilon_0 \mu_0) = \sqrt{\varepsilon'_{yy} \varepsilon'_{xx}}\, \mu'_z/(\varepsilon_0 \mu_0). \tag{25}$$

It can be easily checked that in this case $\varepsilon'_{xx} \varepsilon'_{yy} \simeq \varepsilon_0^2$ and thus the effective refractive index in this case is dependent on the chosen mesh only, as in (21)

$$n'^2 \simeq \mu'_z/\mu_0 = \frac{1}{\det(J)}. \tag{26}$$

The analysis for the H-polarization indicates that a properly selected magnetic material can control these waves, similar to how a dielectric material can control the E-polarized waves. Thus the designer can generate a mesh under the assumptions specified in this section, calculate the refractive index distribution from (23), and choose either tuning ε or μ to operate over E-polarization or H-polarization respectively.

III. The Flat Reflector

The parabolic reflector antenna is one of the most widely applied antennas. In this section, we use the scheme of discrete coordinate transformation to design a flat reflector. The conventional device and the transformed device are shown in Fig. 3.

The conventional reflector has an aperture of 180 mm and a focal length of 109 mm. The central working frequency is 8 GHz, with a wavelength of $\lambda = 37.5$ mm in free space. Coordinate transformation is applied in a region of 300 mm $\times$ 75 mm, and the meshes in the two coordinate systems are shown in Fig. 3. The meshes are chosen so that the FWHM of the angle distribution shown in Fig. 5 is minimized to be 1°(3.3%). The permittivity distribution is then calculated according to (23). In Fig. 6(a), the permittivity map consists of 64 $\times$ 16 square blocks. The transformation produces dispersive values (less than unity) around $x = 80$ mm and $x = -80$ mm. Since the area covered by the dispersive values inside the reflector's aperture is less than 1/2 wavelength, we can approximately set the dispersive values to be one, as illustrated in Fig. 6(b). In addition, a low-resolution map is also generated, which consists of 16 $\times$ 3 larger blocks with dimensions comparable to the wavelength. Since the incident wave cannot resolve the media's properties when their sizes are similar to or smaller than the wavelength, we expect the two maps with different resolutions have similar performances. This was shown for a ground-plane cloak in [22] and will also be shown later through simulations. Fig. 6(c) shows the dispersive low resolution map and Fig. 6(d) shows the approximate non-dispersive map without values less than unity. Table I presents the explicit values of the relative permittivity map depicted in Fig. 6(c). Because the map is symmetric, only the left half of the values are shown in the table.

The FDTD method is used to compare the performances of the devices. In our case, the simulation domain is relatively small and a conventional Cartesian mesh is fine enough to accurately model the devices. A spatial resolution of $\lambda/45$ is chosen [29], [30]. The total-field/scattering-field technique is applied to implement an incident plane wave [31]. Perfectly matched layer absorbing boundary conditions surrounds the devices in order to terminate the simulation domain. This boundary condition matches well most kinds of media and reduces the reflections efficiently [32].

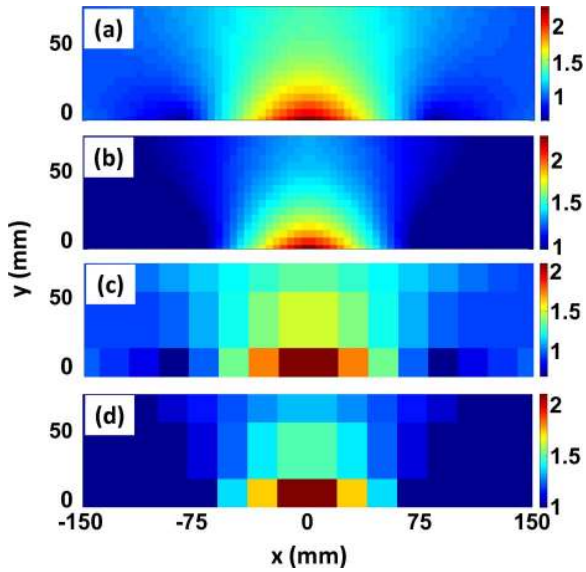

Fig. 6. (a) Permittivity map consisting of 64 $\times$ 16 blocks. (b) Permittivity map consisting of 64 $\times$ 16 blocks, without less-than-unity values. (c) Permittivity map consisting of 16 $\times$ 3 blocks. (d) Permittivity map consisting of 16 $\times$ 3 blocks, without less-than-unity values.

TABLE I
Relative Permittivity Values of the 16 $\times$ 3 Dielectric Blocks (Left Half)

		Column							
		1	2	3	4	5	6	7	8
Row	1	0.94	0.97	1.01	1.07	1.14	1.21	1.28	1.34
	2	0.96	0.96	0.96	1.00	1.10	1.24	1.39	1.49
	3	1.00	0.92	0.84	0.69	0.98	1.37	1.74	2.11

First, a plane wave with E polarization is incident along the y direction at 8 GHz, in order to compare the focal length of the conventional reflector with the focal length of the transformed flat reflector, using the low-resolution permittivity map shown in Fig. 6(d). Fig. 7(a) and (b) illustrates the real part of the E_z field of the transformed flat reflector and the conventional metallic reflector, respectively, after steady-state is reached. For plane wave incidence, both the conventional reflector and the flat reflector focus the energy at their focal points. The two focal lengths are 102.6 mm and 102.7 mm, respectively. In addition, we observe slightly different refraction patterns on sides of the reflectors. These mainly originate after neglecting the negative values in the permittivity map derived from the coordinate transformation.

We also compare the performance of these two devices by using a small horn antenna as a feed, located at the focal points of the reflectors. Fig. 7(c) and (d) compares the performances between the low-resolution flat reflector and a conventional reflector. The field distributions illustrated are indeed similar, which indicates that the flat reflector can excellently transform an incident spherical wave to a plane wave, achieving highly directive radiation.

To investigate the directivity of the devices, in Fig. 8 the radiation patterns of the conventional reflector, the flat reflectors with different resolutions, and the radiation pattern of a flat PEC sheet alone, are compared. The near-to-far-field (NTFF) transformation is applied [31] to observe the far-field characteristics of the

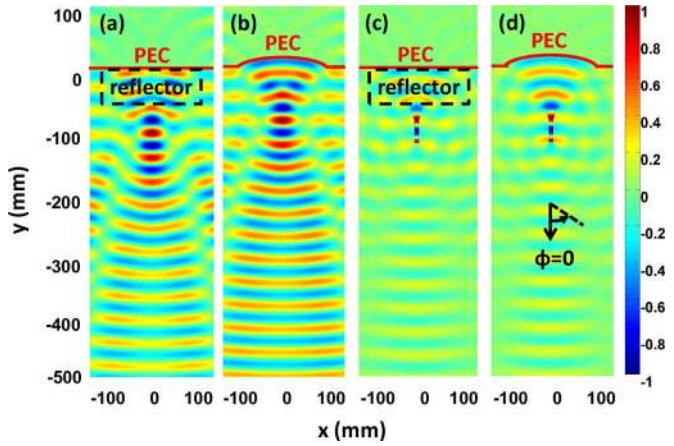

Fig. 7. The real part of the Ez field at 8 GHz. (a) The plane wave illuminates along the y direction to a flat reflector with low resolution. The focal length (measured from the focal point to the center of the PEC) is 102.6 mm.(b) The plane wave illuminates along the y direction to a conventional reflector. The focal length is 102.7 mm. The two focal lengths are very close to each other. (c) A small horn antenna is applied at the focal point to feed the flat reflector. (d) A small horn antenna is applied at the focal point to feed the conventional reflector. The incident waves are reflected and similar quasi-plane waves are observed.

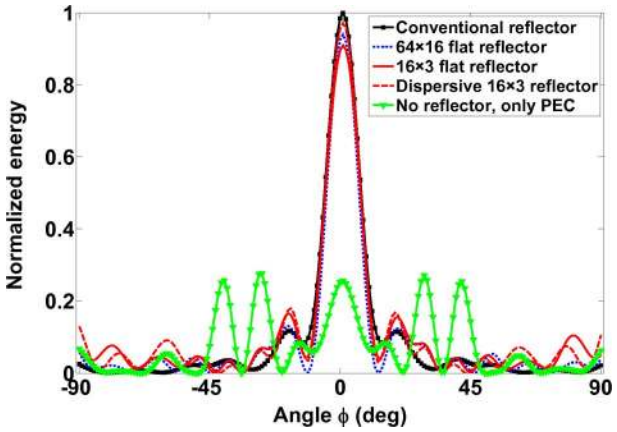

Fig. 8. The comparison of the radiation patterns at 8 GHz. The definition of Φ is shown in Fig. 7(d). The conventional reflector and the two flat reflectors have similar high directivities in the primary angle.

radiation patterns. Using the data obtained from the near-field simulation, the NTFF transformation calculates the forward radiation patterns of the reflectors. The energy is calculated as $|E_z|^2$, and normalized to the peak energy of the conventional reflector. It is shown in Fig. 8 that the conventional reflector and the two flat reflectors produce similarly high directivities around $\phi = 0$, which verifies the excellent cylindrical-to-plane wave transformation. The low resolution flat reflector exhibits slightly worse performance compared to the high resolution one. The low resolution flat reflector with dispersive values has similar pattern as the non-dispersive one, but a little better directivity around $\phi = 0$. Finally, the directivity of the bare PEC sheet is extremely low, as expected.

Furthermore, the bandwidth of the dispersive and non-dispersive flat reflectors is tested at different frequencies. The flat reflectors are both composed by 16×3 large blocks, and the testing frequencies are 4 GHz, 6 GHz, 10 GHz and 12 GHz.

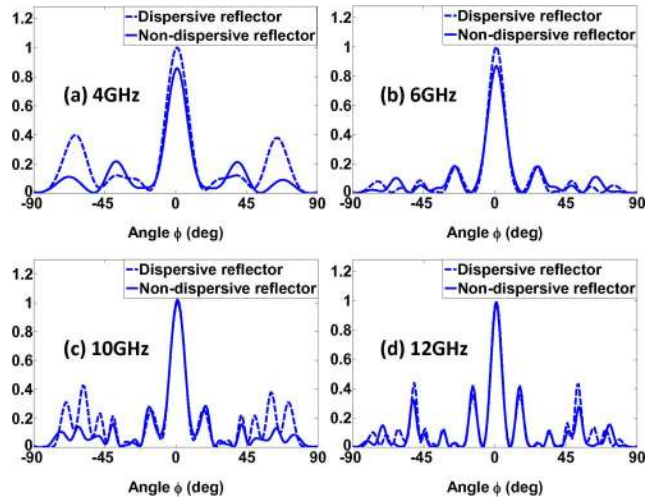

Fig. 9. The comparison of the radiation patterns between dispersive and non-dispersive flat reflectors at 4 GHz, 6 GHz, 10 GHz and 12 GHz. The dispersive reflector has better performance around the designed frequency of 8 GHz, but larger side-lobes than the non-dispersive one when the working frequency goes higher or lower. Both the flat reflector are composed of 16×3 blocks.

Fig. 9 implies that at the frequencies near 8 GHz, the dispersive reflector has the better scattering pattern with higher energy around $\phi = 0$ and low side-lobes. When the operating frequency moves lower or higher, the dispersive reflector has the worse scattering pattern since the side-lobes increase remarkably. It is because when the operating frequency varies away from 8 GHz, the permittivity of the dispersive reflector changes according to the Drude model. As a result, a non-dispersive reflector has comparable performance and wider bandwidth, and much easier to be realized.

From the point of view of the practical realization, the reflections at the feed are also tested to measure the backscattering of the reflector systems. The systems are stimulated by launching a wideband Gaussian pulse with a fixed bandwidth between 6–12 GHz inside the small feed horn. The electric field Ez are recorded at the feeding point, and the excitation pulse is isolated from the reflected signal. The reflection coefficient, which is the ratio of the reflected signal over the input signal, can be seen in Fig. 10. The reflection curves have similar shapes when the conventional reflector, the 64×16 flat reflector and the 16×3 flat reflectors are applied. Nevertheless the reflection increases with the designed flat reflectors. This is reasonable because the impedance mismatch at the interfaces between the air and the dielectric blocks result in higher reflections. However, the two flat reflectors still have similar good performances over the frequency range. Some fluctuations are observed over the bandwidth. But according to the performance of the conventional reflector, the reflector system itself is also frequency dependant, so the fluctuations are not from the designed flat reflectors. In other words, the bandwidth of the transformation-based flat reflectors is not affected significantly.

IV. The Flat Lens

In this section we present a design for a flat lens, as a second example of the discrete coordinate transformation. A conventional convex lens, as shown in Fig. 11(a), transforms a point

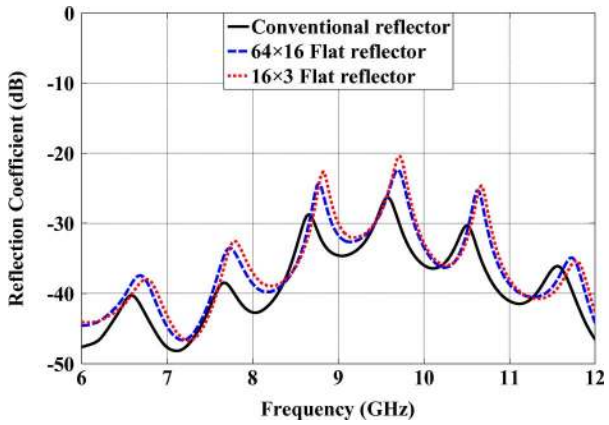

Fig. 10. The comparison of the reflections between the conventional reflector and the two flat reflectors over 6–12 GHz. The reflector systems are stimulated by a wideband Gaussian pulse.

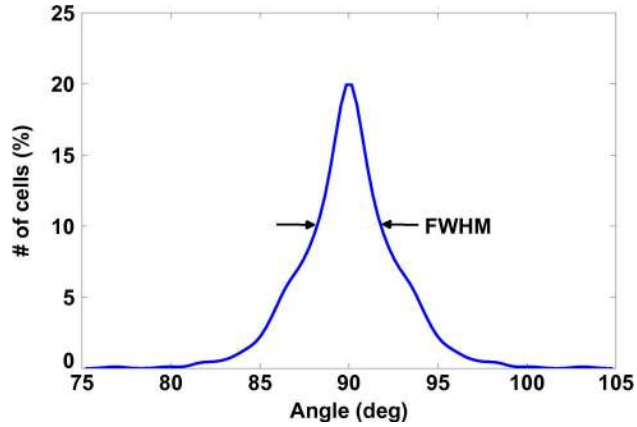

Fig. 12. The distribution of the degrees between two local coordinates in every grid of the virtual space. In this case the FWHM index is 3.6°, indicating that most of the local coordinates are quite orthogonal.

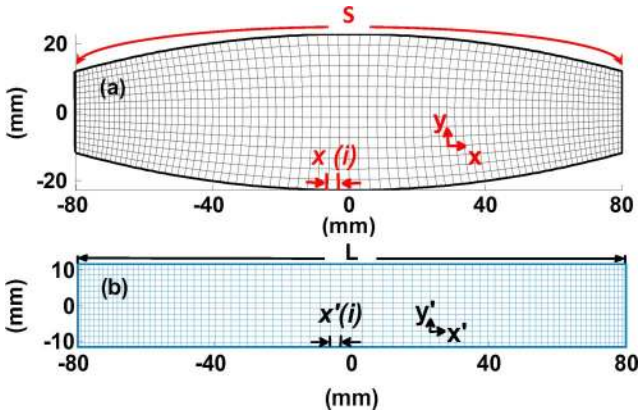

Fig. 11. (a) The virtual space with distorted coordinates. The whole space is a convex lens made of dielectric with the relative permittivity of 3. (b) The physical space with Cartesian coordinates. The whole space is a transformed flat lens.

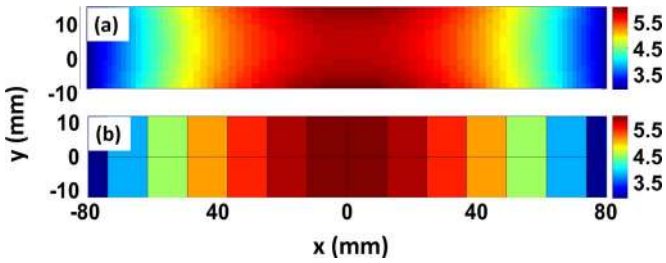

Fig. 13. The permittivity maps of the flat lens. (a) The map consisting of 80 × 15 blocks. (b) The map consisting of 14 × 2 blocks.

TABLE II
RELATIVE PERMITTIVITY VALUES OF THE 14 × 2 DIELECTRIC BLOCKS (LEFT HALF)

		Column						
		1	2	3	4	5	6	7
Row	1	3.11	3.89	4.56	5.12	5.52	5.83	5.96
	2	3.11	3.89	4.56	5.12	5.52	5.83	5.96

source located at its focal point to a plane wave at the other side. In this scenario the lens has a thickness of 45.6 mm at its center and an aperture of 160 mm, and is made from an isotropic medium with a relative permittivity equal to 3. The transformed flat lens is designed to have the same aperture but a much smaller thickness of 23.8 mm, as shown in Fig. 11(b).

Here we focus on the E-polarized incident waves. A similar process is applied to design the all-dielectric flat lens. Contrary to the case of the flat reflector discussed in the previous section, the top and bottom boundaries in the virtual space are curved lines. To achieve a good orthogonality, the points are no longer averagely distributed on these lines. More points assemble at the four corners, resulting in smaller cells at the two sides and larger cells in the central region. In the physical space, the points on the top and bottom boundaries are determined in the same proportion as in the virtual space. Note that since some cells in the physical space are not squares, the components of μ_{xx} and μ_{yy} have quite different values, implying the background material in the physical space is more anisotropic. Strictly speaking, the effective average refractive index has approximate values of $n'^2 \simeq (1)/(\det(J))$ in the central area and at the two ends. However, for an incidence whose incident angle of ϕ is not very large, the isotropic approximation is acceptable, and the flat lens holds its performances, as will be demonstrated in this section.

A near-orthogonal grid is generated in the virtual space. The covariant metric g is calculated for each cell, in accordance with the procedure described in the previous section. Fig. 12 shows the corresponding angle that determines the orthogonality of each cell. The FWHM is 3.6°(12%), implying that the coordinate system is fairly orthogonal and the proposed technique can be applied. The non-orthogonal cells which remain at the edges of the distribution in Fig. 12 are the ones located near the edges of the lens in the virtual space of Fig. 11(a). Within this approximation, we assume, as before, that $\partial x/\partial y$ and $\partial y/\partial x$ remain approximately close to zero.

In Fig. 13 the resulting permittivity maps for different grid resolutions are presented, calculating using (23) as before. The map in Fig. 13(a) has a high resolution of 80 × 15 blocks and the map in Fig. 13(b) has a low resolution of 14 × 2 blocks. The exact values of the relative permittivity map of Fig. 13(b) are reported in Table II. Because the map is symmetric, only the values for the left half of the map are provided.

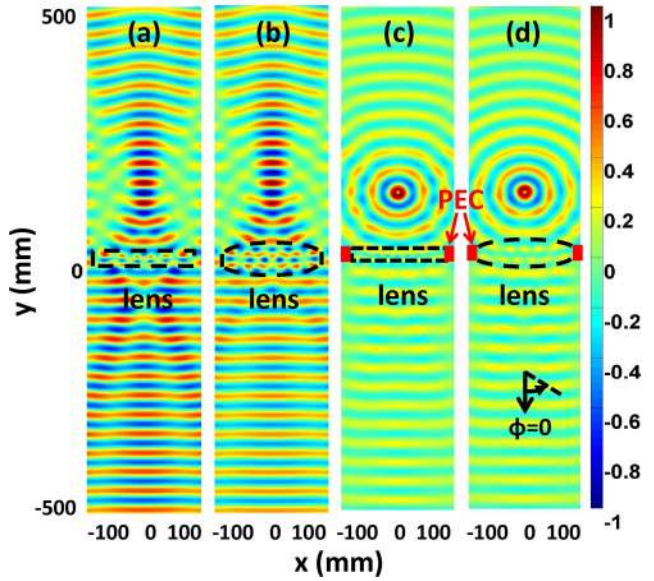

Fig. 14. The real part of the Ez field at 8 GHz. (a) The plane wave illuminates along the y direction to the flat lens. The focal length is 130 mm. (b) The plane wave illuminates along the y direction to the conventional lens. The focal length is 131 mm. The two focal points are very close to each other. (c) A point source is applied at the focal point to feed the flat lens with low resolution. (d) A point source is applied at the focal point to feed the conventional lens. On the other sides, similar quasi-plane waves are detected.

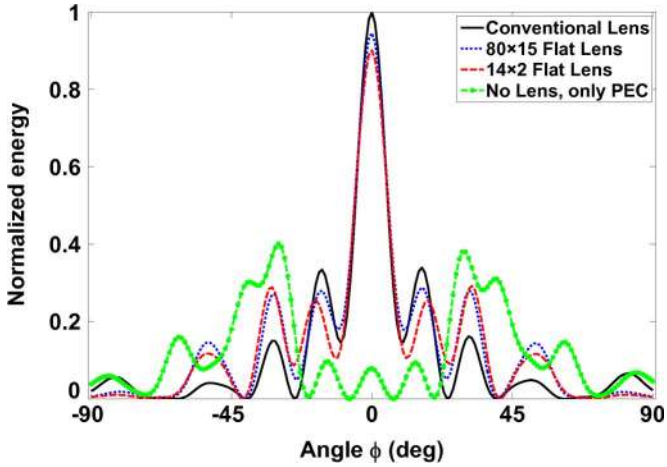

Fig. 15. The comparison of the radiation patterns at 8 GHz. The definition of Φ is shown in Fig. 13(d). The conventional lens and the two flat lenses have similar high directivities in the primary angle.

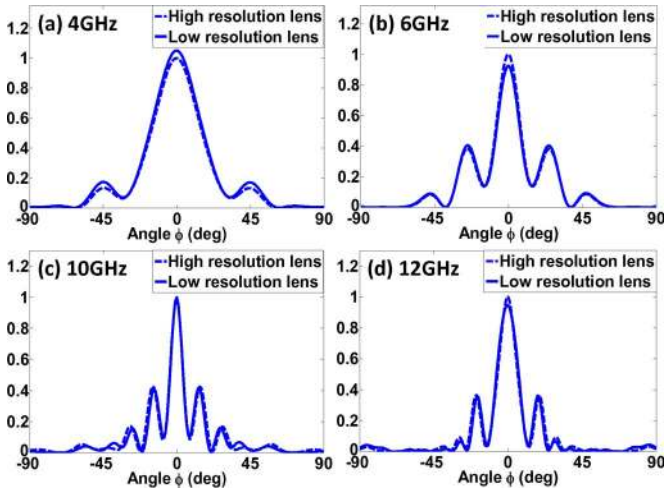

Fig. 16. The comparison of the radiation patterns between high resolution (80×15 blocks) and low resolution (14×2 blocks) flat lenses at 4 GHz, 6 GHz, 10 GHz and 12 GHz. They have similar performances over the frequencies.

In order to test the performance of the designed flat lens, FDTD simulations are performed. In Fig. 14 the real part of the electric field E_z are shown for different types of excitation. To test the focusing properties of the flat lens, we compare its field distribution [Fig. 14(a)] with the field distribution of the conventional convex lens [Fig. 14(b)], when a plane wave along the $+y$ direction illuminates the devices. The waves focus at a focal length of 130 mm for the flat lens, which is very close to the original focal length of 131 mm for the conventional lens.

Next, line sources are placed on the focal points of the two devices in order to observe plane wave generation on the other side of the lenses. Two blocks of PEC are added on either side of the lenses to prevent interference from leaky waves. Fig. 14(c) and (d) depict the real part of the E_Z field when a low-resolution flat lens and a conventional lens are used, respectively. Indeed, plane waves are seen to emerge on the other side of the sources, which verifies the excellent performance of the simplified all-dielectric flat lens. Note also that the reflected waves are slightly stronger on the $y > 0$ side for the case of the simplified flat lens. This occurs because blocks with large values of permittivity are located at the center of the flat lens, thus the interface between the air and the flat lens is mismatched even more. This issue can be mediated by adding an impedance matched layer between the source and the lens.

Fig. 15 depicts a comparison of the radiation patterns of the conventional lens, the flat lenses with different resolutions, and also the pattern when lenses are removed and the PEC blocks are left alone. The conventional lens and the two flat lenses have very similar high directivities along their optical axes, with the low resolution flat lens having a slightly worse performance than the high resolution one. When all the lenses are removed, the directivity decreases dramatically. The energy then splits on the two sides because of the reflections of the PEC blocks.

Further more, the bandwidth of the high resolution flat lens and low resolution flat lens is tested at different frequencies of 4 GHz, 6 GHz, 10 GHz and 12 GHz. Fig. 16 implies that the flat lenses with different resolutions have pretty similar radiation patterns over the frequencies. At low frequency, the major lobe becomes wider. The directivity is obvious from 4 GHz to 12 GHz, which verifies the cylindrical-to-plane wave transformation through the flat lenses over a wide band.

The reflections at the feed are also tested to measure the backscattering of the lenses. The devices are stimulated by wideband Gaussian pulses with a fixed bandwidth between 2–14 GHz at the focal points and the reflections can be seen in Fig. 17. The reflection curves have similar shapes when the conventional lens, the 80×15 flat lens and the 14×2 flat lens are applied. But the reflection increases with the designed flat

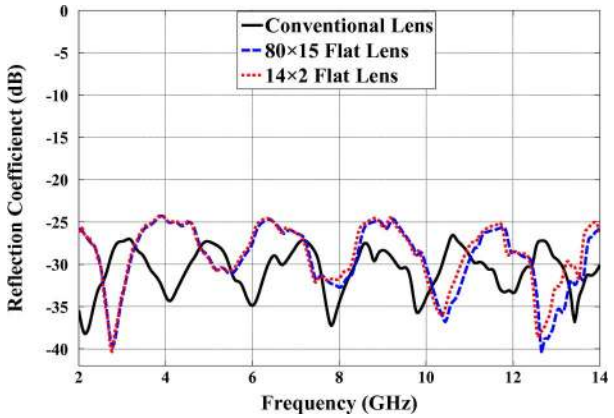

Fig. 17. The comparison of the reflections between the conventional lenses and the two flat lenses over 2–14 GHz. The lenses are stimulated by a wideband Gaussian pulse.

lenses. This is because at the central part of the flat lenses, the permittivities are much higher than the value in the conventional lens, which causes an increased impedance mismatch at the interfaces between the air and the lens. However, the two flat lenses still have similar good performances over the frequency range. Furthermore, some fluctuations are observed over the bandwidth. But according to the performance of the conventional lens, the convex lens itself is frequency dependent. In other words, the bandwidth of the device is not affected by the transformation-based flat lens design. It could be explained in a physical way that as long as the wavelength is larger than the individual blocks (where the effective medium approach is valid), the bandwidth is not affected because the wave sees an isotropic material with continuously varying permittivity. This was shown for the similarly-designed carpet cloak in [22].

V. Conclusion

Concluding, the proposed discrete coordinate transformation provides a scheme to transform the conventional antennas with curved shapes into all-dielectric flat ones. Once the near-orthogonal meshes are carefully generated, the media can be isotropic and realize all-dielectric devices for E polarization. Reasonable approximations and simplifications are introduced in the design to simplify the construction of the devices, without significantly sacrificing their performance. A flat reflector and a flat lens are designed as examples. FDTD simulation results demonstrate good agreement between the transformed devices and the conventional ones.

References

[1] J. B. Pendry, D. Schurig, and D. R. Smith, "Controlling electromagnetic fields," *Science*, vol. 312, pp. 1780–1782, 2006.
[2] U. Leonhardt, "Optical conformal mapping," *Science*, vol. 312, p. 17771780, 2006.
[3] D. Schurig, J. B. Pendry, and D. R. Smith, "Calculation of material properties and ray tracing in transformation media," *Opt. Express*, vol. 14, no. 21, pp. 9794–9804, 2006.
[4] W. Cai, U. Chettiar, A. Kildishev, V. Shalaev, and G. Milton, "Nonmagnetic cloak with minimized scattering," *Appl. Phys. Lett.*, vol. 91, p. 111105, 2007.
[5] W. Jiang, J. Chin, Z. Li, Q. Cheng, R. Liu, and T. Cui, "Analytical design of conformally invisible cloaks for arbitrarily shaped objects," *Phys. Rev. E*, vol. 77, no. 6, p. 66607, 2008.
[6] Y. Lai, H. Chen, Z. Zhang, and C. Chan, "Complementary media invisibility cloak that cloaks objects at a distance outside the cloaking shell," *Phys. Rev. Lett.*, vol. 102, no. 9, p. 93901, 2009.
[7] D. Schurig, J. J. Mock, B. J. Justice, S. A. Cummer, J. B. Pendry, A. F. Starr, and D. R. Smith, "Metamaterial electromagnetic cloak at microwave frequencies," *Science*, vol. 314, pp. 977–980, 2006.
[8] Y. Luo, H. Chen, J. Zhang, L. Ran, and J. Kong, "Design and analytical full-wave validation of the invisibility cloaks, concentrators, and field rotators created with a general class of transformations," *Phys. Rev. B*, vol. 77, no. 12, p. 125127, 2008.
[9] M. Rahm, D. Schurig, D. Roberts, S. Cummer, D. Smith, and J. Pendry, "Design of electromagnetic cloaks and concentrators using form-invariant coordinate transformations of Maxwells equations," *Photon. Nanostruct. Fundam. Appl.*, vol. 6, no. 1, pp. 87–95, 2008.
[10] W. Jiang, T. Cui, H. Ma, X. Zhou, and Q. Cheng, "Cylindrical-to-planewave conversion via embedded optical transformation," *Appl. Phys. Lett.*, vol. 92, p. 261903, 2008.
[11] A. Alù and N. Engheta, "Cloaking a sensor," *Phys. Rev. Lett.*, vol. 102, no. 23, p. 233901, 2009.
[12] B. Vasić, G. Isić, R. Gajić, and K. Hingerl, "Coordinate transformation based design of confined metamaterial structures," *Phys. Rev. B*, vol. 79, no. 8, p. 85103, 2009.
[13] P. Tichit, S. Burokur, and A. de Lustrac, "Ultradirective antenna via transformation optics," *J. Appl. Phys.*, vol. 105, no. 10, p. 4912, 2009.
[14] Y. Luo, J. Zhang, H. Chen, J. Huangfu, and L. Ran, "High-directivity antenna with small antenna aperture," *Appl. Phys. Lett.*, vol. 95, p. 193506, 2009.
[15] J. Pendry, A. Holden, W. Stewart, and I. Youngs, "Extremely low frequency plasmons in metallic mesostructures," *Phys. Rev. Lett.*, vol. 76, no. 25, pp. 4773–4776, 1996.
[16] J. Pendry, A. Holden, D. Robbins, and W. Stewart, "Magnetism from conductors and enhanced nonlinear phenomena," *IEEE Trans. Microw. Theory Tech.*, vol. 47, no. 11, pp. 2075–2084, 1999.
[17] J. Li and J. Pendry, "Hiding under the carpet: A new strategy for cloaking," *Phys. Rev. Lett.*, vol. 101, no. 20, p. 203901, 2008.
[18] R. Liu, C. Ji, J. J. Mock, J. Y. Chin, T. J. Cui, and D. R. Smith, "Broadband ground-plane cloak," *Science*, vol. 323, no. 5912, pp. 366–369, 2009.
[19] J. Valentine, J. Li, T. Zentgraf, G. Bartal, and X. Zhang, "An optical cloak made of dielectrics," *Nat. Mater.*, vol. 8, pp. 568–571, 2009.
[20] L. Gabrielli, J. Cardenas, C. Poitras, and M. Lipson, "Silicon nanostructure cloak operating at optical frequencies," *Nat. Phot.*, vol. 3, no. 8, pp. 461–463, 2009.
[21] J. Lee, J. Blair, V. Tamma, Q. Wu, S. Rhee, C. Summers, and W. Park, "Direct visualization of optical frequency invisibility cloak based on silicon nanorod array," *Opt. Express*, vol. 17, no. 15, pp. 12 922–12 928, 2009.
[22] E. Kallos, C. Argyropoulos, and Y. Hao, "Ground-plane quasicloaking for free space," *Phys. Rev. A*, vol. 79, no. 6, p. 63825, 2009.
[23] F. Kong, B. Wu, J. Kong, J. Huangfu, S. Xi, and H. Chen, "Planar focusing antenna design by using coordinate transformation technology," *Appl. Phys. Lett.*, vol. 91, p. 253509, 2007.
[24] D. Roberts, N. Kundtz, and D. Smith, "Optical lens compression via transformation optics," *Opt. Express*, vol. 17, no. 19, pp. 16 535–16 542, 2009.
[25] N. Kundtz and D. Smith, "Extreme-angle broadband metamaterial lens," *Nat. Mater.*, vol. 9, pp. 129–132, 2010.
[26] J. Thompson, B. Soni, and N. Weatherill, *Handbook of Grid Generation*. Boca Raton, FL: CRC, 1999.
[27] R. Holland, "Finite-difference solution of Maxwell's equations in generalized nonorthogonal coordinates," *IEEE Trans. on Nuclear Science*, vol. 30, pp. 4589–4591, 1983.
[28] Y. Hao and C. Railton, "Analyzing electromagnetic structures with curved boundaries on Cartesian FDTD meshes," *IEEE Trans. Microwave Theory Tech.*, vol. 46, pp. 82–88, 1998.
[29] Y. Zhao, C. Argyropoulos, and Y. Hao, "Full-wave finite-difference time-domain simulation of electromagnetic cloaking structures," *Opt. Express*, vol. 16, no. 9, pp. 6717–6730, 2008.
[30] C. Argyropoulos, Y. Zhao, and Y. Hao, "A radially-dependent dispersive finite-difference time-domain method for the evaluation of electromagnetic cloaks," *IEEE Trans. Antennas Propag.*, vol. 57, no. 5, pp. 1432–1441, May 2009.
[31] A. Taflove and S. C. Hagness, *Computational Electrodynamics: The Finite-Difference Time-Domain Method*, 3rd ed. Boston, MA: Artech House, 2005.
[32] J.-P. Bérenger, "A perfectly matched layer for the absorption of electromagnetic waves," *J. Comp. Phys.*, vol. 114, pp. 185–200, 1994.

Wenxuan Tang (S'10) received the Bachelor degree in electronic engineering and the M.Sc. degree in electromagnetic field and microwave technology from Southeast University, Nanjing, China, in 2006 and 2009, respectively. She is currently working toward the Ph.D. degree at Queen Mary University of London, London, U.K.

Her main research interests include FDTD-based electromagnetic modelling, metamaterials and their novel applications, and transformation electromagnetics. She has published eight technical papers in journals and some established international conferences.

Christos Argyropoulos (S'04) received the Diploma of Electrical and Computer Engineering from the Aristotle University of Thessaloniki, Greece, in 2006, and the M.Sc. degree in communication engineering from the University of Manchester, Manchester, U.K., in 2007. He is currently working towards the Ph.D. degree at Queen Mary University of London, London, U.K.

His main research interests include computational electromagnetics, numerical and analytical modeling of metamaterials and their applications, transformation electromagnetics, plasmonics and antennas design. He has published over 30 technical papers and book chapters in highly ranked journals, refereed conference proceedings and scientific books. Some of the papers have been published in *Optics Express, Physical Review A and E*, and the IEEE TRANSACTIONS ON ANTENNAS AND PROPAGATION. He has strong experience in computational electromagnetics, notably in the area of finite-difference time-domain (FDTD) method for metamaterials and coordinate transformation based devices.

Mr. Argyropoulos has served as a reviewer for *Optics Express*, the IEEE TRANSACTIONS ON ANTENNAS AND PROPAGATION, *Progress In Electromagnetics Research (PIER)* and the *Journal of Electromagnetic Waves and Applications (JEMWA)*.

Efthymios Kallos received the Diploma in electrical engineering from the National Technical University of Athens, Athens, Greece, in 2003 and the Ph.D. degree in electrical engineering from the University of Southern California, Los Angeles, in 2008.

He is currently a Postdoctoral Researcher with Queen Mary University of London, London, U.K., working on metamaterial-based electromagnetic cloaking devices. His interests range from plasmas and high-energy physics to electromagnetics and antenna design.

Wei Song received the Bachelor degree in telecommunications from Northeastern University, China, in 2002, and the M.Sc. degree in telecommunication and Ph.D. degree in electromagnetics from Queen Mary University of London, London, U.K., in 2003 and 2008, respectively.

She then worked as a Postdoctoral Research Assistant at the Antennas and Electromagnetic Research Group, Queen Mary. In December 2008, she joined the Center for Electromagnetic Simulation, School of Information and Electronic, Beijing Institute of Technology (BIT), Beijing, China, as a lecturer. Her research interests include computational electromagnetics, scattering, and metamaterial analysis, etc.

Yang Hao (M'00–SM'06), received the Ph.D. degree from the University of Bristol, Bristol, U.K., in 1998.

From 1998 to 2000, he was a Postdoctoral Research Fellow with the School of Electrical and Electronic Engineering, University of Birmingham, U.K. In May 2000, he joined the Antenna Engineering Group, Queen Mary College, University of London, London, U.K., first as a Lecturer and was promoted to Reader in 2005, and Professor in 2007. He is active in a number of areas including computational electromagnetics, electromagnetic bandgap structures and microwave metamaterials, antennas and radio propagation for body centric wireless networks, active antennas for millimeter/submillimeter applications and photonic integrated antennas. He is a co-editor and coauthor of the books *Antennas and Radio Propagation for Body-Centric Wireless Communications* (Boston, MA: Artech House, 2006), and *FDTD modelling of Metamaterials: Theory and Applications* (Boston, MA: Artech House, 2008), respectively.

Prof. Hao was elected as a Fellow of the ERA Foundation in 2007 and a Fellow of IET in 2010. He is an Associate Editor for the *IEEE Antennas and Wireless Propagation Letters* and IIEEE TRANSACTIONS ON ANTENNAS AND PROPAGATION. He was also a Co-Guest Editor for the IEEE TRANSACTIONS ON ANTENNAS AND PROPAGATION. He is a member of the Executive Team of IET Antennas and Propagation Professional Network and a member of the "New Emerging Technology" Committee of the IEEE Antenna and Propagation Society. He is also a member of Board of the European School of Antenna Excellence, a member of EU ASSIST Cost Action and the Virtual Institute for Artificial Electromagnetic Materials and Metamaterials, "Metamorphose VI AISBL." He has served as an invited (ISAP'07, LAPC'07, IWAT'08) and keynote speaker (ANTEM'05, IWAT'10), a conference General Chair (LAPC'08, Metamaterials'09), a Session Chair and short course organizer at many international conferences.